Friction **10**(10): 1660–1675 (2022)
https://doi.org/10.1007/s40544-021-0580-7
ISSN 2223-7690
CN 10-1237/TH
RESEARCH ARTICLE

Description of sand–metal friction behavior based on subloading-friction model

Toshiyuki OZAKI[1], **Yuki YAMAKAWA**[2,*], **Masami UENO**[3], **Koichi HASHIGUCHI**[4,5]

[1] *Kyushu Electric Engineering Consultants Inc., Fukuoka 810-0005, Japan*

[2] *Department of Civil and Environmental Engineering, Tohoku University, Sendai 980-8579, Japan*

[3] *University of the Ryukyus, Okinawa 903-0213, Japan*

[4] *MSC Software Ltd., Tokyo 101-0054, Japan*

[5] *Kyushu University, Fukuoka 819-0395, Japan*

Received: 08 June 2021 / Revised: 19 October 2021 / Accepted: 01 Decmeber 2021

Abstract: A subloading-friction model is formulated to describe the smooth transient variation from static friction to kinetic friction, the recovery to static friction after the sliding velocity decreases, and the accumulation of sliding displacement under the cyclic loading of contact stress. In the past relevant studies, however, the model formulation used for simulations is limited to the hypoelastic-based plasticity framework, and the validation of the model is limited to simulations of the test data for metal-to-metal friction. In this study, the formulation of the subloading-friction model based on a hyperelastic-based plasticity framework is adopted. In the fields of civil, geotechnical, agricultural engineering, and terramechanics, the interaction between soils and metals is critical, as reflected in construction and agricultural machinery, foundation piles, and retaining walls. The validity of the model for describing the friction between various sands and metals is verified by simulations of the experimental data under monotonic and cyclic loadings.

Keywords: subloading-friction model; sand–metal friction; monotonic/cyclic sliding; static/kinetic friction

1 Introduction

It is well acknowledged that (1) when a body at rest begins to slide, a high friction coefficient appears first, which is known as static friction; (2) subsequently, the friction coefficient decreases toward its lowest stationary value, which is known as kinetic friction; (3) when the sliding suspends and then restarts, the friction coefficient approaches the static friction coefficient, and a behavior similar to the initial sliding is observed [1–10]. The magnitude of the difference between static friction and kinetic friction can reach up to several tens of percent, depending on the materials as well as the sliding velocity and stress levels [11]. Hence, a mathematical model that considers these characteristics is required in engineering analyses involving frictional boundaries.

The recovery of the static friction coefficient has been investigated theoretically and modeled via mathematical expressions directly including the elapsed time after sliding ceases [2, 3, 6–8, 10]. However, the evaluation of the duration of sliding suspension is often accompanied by the ambiguity in judging when sliding ceases and restarts, particularly when the sliding velocity varies gradually within a low velocity range. Therefore, the inclusion of the duration time of sliding suspension in the constitutive modeling of the friction law may result in the loss of objectivity [12]. Meanwhile, the variation in frictional properties on the contact surfaces, including the above-mentioned transitional behavior, should be expressed in terms of the contact traction, sliding

* Corresponding author: Yuki YAMAKAWA, E-mail: yuki.yamakawa.c7@tohoku.ac.jp

velocity, and internal variables representing the state and/or history of a sliding process without including the suspension duration.

In the 1970s and early 1980s, the "rate-and-state friction" (RSF) approach was proposed for modeling static and kinetic friction. Dieterich [13–15] proposed a function for the friction coefficient based on the time of the stationary contact and the sliding velocity, as well as discussed the mechanics of stick–slip. Ruina and Rice [16, 17] proposed a friction law that depends on the state and slip history by introducing internal state variables. Meanwhile, Popova and Popov [18] presented a historical overview of studies pertaining to friction laws proposed in early works by Coulomb and Amontons, as well as subsequent developments leading to the RSF approach. However, the RSF model was formulated in terms of scalar-valued quantities based on only one-dimensional considerations. Therefore, the application of RSF models is limited to one-dimensional linear sliding.

For general three-dimensional engineering analyses, a friction model applicable to multidirectional frictional sliding on a contact surface is required. In this regard, constitutive relations to describe multi-dimensional frictional sliding have been formulated in the framework of elastoplasticity (e.g., Refs. [19, 20]). The key idea of the friction models based on the elastoplastic approach is twofold: (1) the decomposition of the sliding displacement into an elastic (reversible or stick/adhesive) component and a plastic (irreversible slip) component to formulate plastic internal variables that are irrelevant to elastic sliding but change with the plastic sliding history; (2) the expression of a yield function in terms of the contact traction and internal variables to define the loading criterion of whether plastic sliding proceeds in multi-dimensional sliding processes. Computational treatment of friction constitutive laws within the finite element formulation has been established [21, 22] and is widely used in engineering analyses involving frictional contact.

Within the framework of elastoplasticity theory, the aforementioned fundamental friction behaviors, i.e., the decrease in the friction coefficient from the static to the kinetic friction coefficient via plastic sliding and the recovery of the friction coefficient by the decrease in the sliding velocity, have been formulated in the subloading-friction model [23–25] based on the concept of a subloading surface [26]. In this concept, a subloading surface with a shape and a direction similar to those of the sliding-yield surface is introduced, and the plastic (irreversible) sliding velocity is assumed to be induced gradually as the subloading surface approaches the sliding-yield surface. Consequently, the subloading-friction model is endowed with the capability to describe the gradual evolution of plastic sliding as the contact traction approaches the sliding-yield limit and hence the accumulation of sliding displacement under the cyclic loading of the contact traction inside the sliding-yield surface. The validity of the subloading-friction model for describing actual frictional sliding behavior was verified by comparison with the test data [23–25]. However, the validation of the model in these past studies was limited to the sliding behavior of metal interfaces. Recently, Ozaki et al. [27] demonstrated the applicability of the subloading-friction model to frictional sliding between a rough rubber hemisphere and a smooth acrylic plate.

In the field of civil and geotechnical engineering, the interaction between soils and metals is critical, as reflected in the driving installation process of the pile foundations and their subsidence/loosening under traffic loads, earthquakes, etc. [28–31]; retaining walls; construction machineries; and the effect of friction between a soil specimen and a testing apparatus in laboratory tests for geomaterials [32–34]. In the field of terramechanics, frictional sliding between soils and metals is relevant to the interactions between wheels/blades and soil terrains [35–45]. Extensive experimental research has been performed to precisely measure the friction property of soil–steel interfaces under monotonic or cyclic loading [46–53], and to elucidate the factors affecting the interface friction property, such as the testing methods, materials, sliding velocity, interface roughness, particle geometry, gradation, and grain crushing [54–57]. Recently, advanced experimental investigations on the frictional properties of the geological materials have been conducted, e.g., micromechanical experiments of inter-granule loading [58], sliding friction tests of the interface between shale rock and dry quartz sand particles [59], and granular friction tests under linearly reciprocating sliding [60]. It is noteworthy that a

mathematical model is required for the successful analysis and prediction of problems in these areas. Hence, the abovementioned features of the subloading-friction model are advantageous for describing the multidirectional and cyclic frictional sliding behavior at the interfaces between soils and metals, which are often encountered in the fields of civil and geotechnical engineering, construction and agricultural machinery, and terramechanics. Currently, however, the validation and application of the subloading-friction model are limited to frictional sliding between manufacturing materials and have not been done for soil–metal friction.

In this study, the formulation of the subloading-friction model based on the hyperelastic-based plasticity framework was adopted. The elastic–plastic additive decomposition of the sliding displacement vector is introduced in Section 2. Section 3 describes the hyperelastic equation used to define the relation between the contact traction vector and the elastic (reversible) sliding displacement vector. In the previous subloading-friction models [23–25, 27], a hypoelastic-based plastic sliding formulation was adopted, in which the rate of elastic sliding displacement is associated with the co-rotational (objective) rate of the contact traction vector via a rate or incremental equation of the hypoelastic law [61, 62]. However, the hypoelastic-based framework is limited to the description of frictional sliding involving infinitesimal elastic sliding. Furthermore, it requires a cumbersome time-integration scheme for the rate equation of the hypoelastic law to calculate the sliding displacement vs. the contact traction relationship; hence, meticulous treatment is necessary in the numerical time-integration scheme to guarantee the objectivity of the constitutive relation [63, 64]. More importantly, it is well acknowledged that the hypoelastic-based framework has several serious drawbacks in terms of physical and theoretical aspects, namely, energy dissipation and its accumulation within a purely elastic range during cyclic loadings [65, 66], and the arbitrariness or non-uniqueness regarding the selection of a co-rotational rate [67]. By contrast, the hyperelastic equation defines the direct relation between the contact traction and elastic sliding displacement, intrinsically assuring the objectivity property as the fundamental requirement for constitutive laws. Its computer implementation is simple and straightforward as it does not require a cumbersome time-integration scheme. Consequently, the hyperelastic-based formulation presented herein offers significant advantages in terms of both physical and numerical aspects.

In this study, we assumed an isotropic friction-yield criterion with tangential associative sliding evolution law, particularly to validate the predictive capability of the subloading-friction model for the evolution and accumulation of sliding displacement under monotonic/cyclic loadings. This is further described in Section 4. The validity of the subloading-friction model for the description of the frictional sliding behavior between sands and metals was verified by simulations of various test data under monotonic and cyclic sliding displacements, and the details are presented in Section 5.

2 Sliding displacement and contact traction

We consider the sliding displacement of the counter (slave) body relative to the main (master) body, denoted by $\overline{\boldsymbol{u}}$, and assume that it is decomposed orthogonally into the normal component $\overline{\boldsymbol{u}}_{\mathrm{n}}$ and tangential component $\overline{\boldsymbol{u}}_{\mathrm{t}}$ to the contact surface in the additive form, as Eq. (1):

$$\overline{\boldsymbol{u}} = \overline{\boldsymbol{u}}_{\mathrm{n}} + \overline{\boldsymbol{u}}_{\mathrm{t}} \tag{1}$$

with

$$\begin{cases} \overline{\boldsymbol{u}}_{\mathrm{n}} = \left(\overline{\boldsymbol{u}}\cdot\boldsymbol{n}\right)\boldsymbol{n} = \left(\boldsymbol{n}\otimes\boldsymbol{n}\right)\overline{\boldsymbol{u}} = -\overline{u}_{\mathrm{n}}\boldsymbol{n} \\ \overline{\boldsymbol{u}}_{\mathrm{t}} = \overline{\boldsymbol{u}} - \overline{\boldsymbol{u}}_{\mathrm{n}} = \left(\boldsymbol{I} - \boldsymbol{n}\otimes\boldsymbol{n}\right)\overline{\boldsymbol{u}} \end{cases} \tag{2}$$

where $\boldsymbol{I}$ denotes the second-order identify tensor, $\boldsymbol{n}$ denotes the unit outward normal vector of the surface of the main body, and the normal component is expressed as

$$\overline{u}_{\mathrm{n}} \equiv -\boldsymbol{n}\cdot\overline{\boldsymbol{u}}_{\mathrm{n}} = -\boldsymbol{n}\cdot\overline{\boldsymbol{u}} \tag{3}$$

where the minus sign for $\overline{u}_{\mathrm{n}}$ is introduced to yield a positive number when the counter body approaches the main body.

We assume the additive decomposition of the sliding displacement vector $\overline{\boldsymbol{u}}$ into the elastic sliding displacement $\overline{\boldsymbol{u}}^{\mathrm{e}}$ and the plastic (irreversible) sliding displacement $\overline{\boldsymbol{u}}^{\mathrm{p}}$ in the following form:

$$\overline{\boldsymbol{u}} = \overline{\boldsymbol{u}}^{\mathrm{e}} + \overline{\boldsymbol{u}}^{\mathrm{p}} \tag{4}$$

This additive decomposition exactly holds even for a finite (large) sliding displacement, which is not limited to an infinitesimal range. Subsequently, the elastic and plastic components are further decomposed into normal ($\overline{\boldsymbol{u}}_{\mathrm{n}}^{\mathrm{e}}$, $\overline{\boldsymbol{u}}_{\mathrm{n}}^{\mathrm{p}}$) and tangential components ($\overline{\boldsymbol{u}}_{\mathrm{t}}^{\mathrm{e}}$, $\overline{\boldsymbol{u}}_{\mathrm{t}}^{\mathrm{p}}$), i.e.,

$$\begin{cases} \overline{\boldsymbol{u}}^{\mathrm{e}} = \overline{\boldsymbol{u}}_{\mathrm{n}}^{\mathrm{e}} + \overline{\boldsymbol{u}}_{\mathrm{t}}^{\mathrm{e}} \\ \overline{\boldsymbol{u}}^{\mathrm{p}} = \overline{\boldsymbol{u}}_{\mathrm{n}}^{\mathrm{p}} + \overline{\boldsymbol{u}}_{\mathrm{t}}^{\mathrm{p}} \end{cases} \tag{5}$$

where

$$\begin{cases} \overline{\boldsymbol{u}}_{\mathrm{n}}^{\mathrm{e}} = \left(\overline{\boldsymbol{u}}^{\mathrm{e}} \cdot \boldsymbol{n}\right)\boldsymbol{n} = \left(\boldsymbol{n} \otimes \boldsymbol{n}\right)\overline{\boldsymbol{u}}^{\mathrm{e}} = -\overline{u}_{\mathrm{n}}^{\mathrm{e}}\boldsymbol{n} \\ \overline{\boldsymbol{u}}_{\mathrm{t}}^{\mathrm{e}} = \overline{\boldsymbol{u}}^{\mathrm{e}} - \overline{\boldsymbol{u}}_{\mathrm{n}}^{\mathrm{e}} = \left(\boldsymbol{I} - \boldsymbol{n} \otimes \boldsymbol{n}\right)\overline{\boldsymbol{u}}^{\mathrm{e}} \end{cases} \tag{6}$$

and

$$\begin{cases} \overline{\boldsymbol{u}}_{\mathrm{n}}^{\mathrm{p}} = \left(\overline{\boldsymbol{u}}^{\mathrm{p}} \cdot \boldsymbol{n}\right)\boldsymbol{n} = \left(\boldsymbol{n} \otimes \boldsymbol{n}\right)\overline{\boldsymbol{u}}^{\mathrm{p}} = -\overline{u}_{\mathrm{n}}^{\mathrm{p}}\boldsymbol{n} \\ \overline{\boldsymbol{u}}_{\mathrm{t}}^{\mathrm{p}} = \overline{\boldsymbol{u}}^{\mathrm{p}} - \overline{\boldsymbol{u}}_{\mathrm{n}}^{\mathrm{p}} = \left(\boldsymbol{I} - \boldsymbol{n} \otimes \boldsymbol{n}\right)\overline{\boldsymbol{u}}^{\mathrm{p}} \end{cases} \tag{7}$$

by setting

$$\begin{cases} \overline{u}_{\mathrm{n}}^{\mathrm{e}} = -\boldsymbol{n} \cdot \overline{\boldsymbol{u}}_{\mathrm{n}}^{\mathrm{e}} = -\boldsymbol{n} \cdot \overline{\boldsymbol{u}}^{\mathrm{e}} \\ \overline{u}_{\mathrm{n}}^{\mathrm{p}} = -\boldsymbol{n} \cdot \overline{\boldsymbol{u}}_{\mathrm{n}}^{\mathrm{p}} = -\boldsymbol{n} \cdot \overline{\boldsymbol{u}}^{\mathrm{p}} \end{cases} \tag{8}$$

The elastic sliding displacement vector $\overline{\boldsymbol{u}}^{\mathrm{e}}$ is directly associated with the current contact traction vector $\boldsymbol{f}$ via the hyperelastic equation described in Section 3. The elastic–plastic additive decomposition of the sliding displacement vector in Eq. (4) holds exactly even in a large sliding displacement, which is in contrast to the fact that the deformation gradient tensor, defined by the ratio of the current (deformed) infinitesimal line-element vector to the initial one, must be decomposed into elastic and plastic components in the multiplicative form [26]. Therefore, an exact mathematical description of the finite frictional sliding behavior involving large nonlinear sliding displacements and/or rotations of the soil–metal interface can be accomplished using the hyperelastic-based plastic sliding formulation presented herein.

The contact traction vector $\boldsymbol{f}$ for the main body is additively decomposed into the normal traction vector $\boldsymbol{f}_{\mathrm{n}}$ and tangential traction vector $\boldsymbol{f}_{\mathrm{t}}$, as Eq. (9):

$$\boldsymbol{f} = \boldsymbol{f}_{\mathrm{n}} + \boldsymbol{f}_{\mathrm{t}} = -f_{\mathrm{n}}\boldsymbol{n} + f_{\mathrm{t}}\boldsymbol{t}_{\mathrm{f}} \tag{9}$$

where

$$\begin{cases} \boldsymbol{f}_{\mathrm{n}} \equiv (\boldsymbol{n} \cdot \boldsymbol{f})\boldsymbol{n} = (\boldsymbol{n} \otimes \boldsymbol{n})\boldsymbol{f} = -f_{\mathrm{n}}\boldsymbol{n} \\ \boldsymbol{f}_{\mathrm{t}} \equiv \boldsymbol{f} - \boldsymbol{f}_{\mathrm{n}} = \left(\boldsymbol{I} - \boldsymbol{n} \otimes \boldsymbol{n}\right)\boldsymbol{f} = f_{\mathrm{t}}\boldsymbol{t}_{\mathrm{f}} \quad (\boldsymbol{n} \cdot \boldsymbol{f}_{\mathrm{t}} = 0) \end{cases} \tag{10}$$

with

$$\begin{cases} f_{\mathrm{n}} \equiv -\boldsymbol{n} \cdot \boldsymbol{f} \\ f_{\mathrm{t}} \equiv \boldsymbol{t}_{\mathrm{f}} \cdot \boldsymbol{f} = \| \boldsymbol{f}_{\mathrm{t}} \|, \ \boldsymbol{t}_{\mathrm{f}} \equiv \dfrac{\boldsymbol{f}_{\mathrm{t}}}{\| \boldsymbol{f}_{\mathrm{t}} \|} \ (\boldsymbol{n} \cdot \boldsymbol{t}_{\mathrm{f}} = 0, \ \| \boldsymbol{t}_{\mathrm{f}} \| = 1) \end{cases} \tag{11}$$

where $\boldsymbol{t}_{\mathrm{f}}$ means the unit direction vector of $\boldsymbol{f}_{\mathrm{t}}$. The minus sign for f_{n} is introduced to yield a positive number when compressive traction is exerted on the main body by the counter body.

The contact traction vectors $\boldsymbol{f}$, $\boldsymbol{f}_{\mathrm{n}}$, and $\boldsymbol{f}_{\mathrm{t}}$ can be calculated using the Cauchy stress tensor $\boldsymbol{\sigma}$ applied to the contact bodies using Cauchy's fundamental theorem [26], as Eq. (12):

$$\begin{cases} \boldsymbol{f} = \boldsymbol{\sigma}\boldsymbol{n} \\ \boldsymbol{f}_{\mathrm{n}} = (\boldsymbol{n} \cdot \boldsymbol{\sigma}\boldsymbol{n})\boldsymbol{n} = (\boldsymbol{n} \otimes \boldsymbol{n})\boldsymbol{\sigma}\boldsymbol{n} \\ \boldsymbol{f}_{\mathrm{t}} = (\boldsymbol{I} - \boldsymbol{n} \otimes \boldsymbol{n})\boldsymbol{\sigma}\boldsymbol{n} \end{cases} \tag{12}$$

3 Hyperelastic sliding displacement

We consider the hyperelastic model that defines the relationship between the elastic sliding displacement vector $\overline{\boldsymbol{u}}^{\mathrm{e}}$ and the contact traction vector $\boldsymbol{f}$ via the elastic sliding displacement energy function $\varphi(\overline{\boldsymbol{u}}^{\mathrm{e}})$ as Eq. (13):

$$\boldsymbol{f} = \frac{\partial \varphi(\overline{\boldsymbol{u}}^{\mathrm{e}})}{\partial \overline{\boldsymbol{u}}^{\mathrm{e}}} \tag{13}$$

As a specific functional form of $\varphi(\overline{\boldsymbol{u}}^{\mathrm{e}})$, we adopt the quadratic form as Eq. (14):

$$\varphi(\overline{\boldsymbol{u}}^{\mathrm{e}}) = \overline{\boldsymbol{u}}^{\mathrm{e}} \cdot \overline{\boldsymbol{E}}\,\overline{\boldsymbol{u}}^{\mathrm{e}}/2 \tag{14}$$

where $\overline{\boldsymbol{E}}$ denotes the second-order symmetric tensor of the elastic contact tangent stiffness modulus ($\overline{\boldsymbol{E}} = \overline{\boldsymbol{E}}^{\mathrm{T}}$). In the present formulation, we assume a constant elastic modulus. In this case, substituting Eq. (14) into Eq. (13) yields the linear relationship in Eq. (15):

$$\boldsymbol{f} = \overline{\boldsymbol{E}}\overline{\boldsymbol{u}}^{\mathrm{e}}, \ \overline{\boldsymbol{u}}^{\mathrm{e}} = \overline{\boldsymbol{E}}^{-1}\boldsymbol{f} \tag{15}$$

We assume isotropy for the mechanical properties

of the contact surface. In this case, the frictional property is independent of the sliding direction on the contact surface. We further introduce the normalized rectangular coordinate system, $(\bar{\boldsymbol{e}}_1, \bar{\boldsymbol{e}}_2, \bar{\boldsymbol{e}}_3) = (\bar{\boldsymbol{e}}_1, \bar{\boldsymbol{e}}_2, \boldsymbol{n})$, fixed to the contact surface. Under these settings, the elastic contact tangent stiffness modulus tensor $\bar{\boldsymbol{E}}$, with its inverse tensor, is expressed as Eq. (16):

$$\begin{cases} \bar{\boldsymbol{E}} = \alpha_{\mathrm{t}}(\boldsymbol{I} - \boldsymbol{n}\otimes\boldsymbol{n}) + \alpha_{\mathrm{n}}\boldsymbol{n}\otimes\boldsymbol{n} \\ \quad = \alpha_{\mathrm{t}}(\bar{\boldsymbol{e}}_1\otimes\bar{\boldsymbol{e}}_1 + \bar{\boldsymbol{e}}_2\otimes\bar{\boldsymbol{e}}_2) + \alpha_{\mathrm{n}}\boldsymbol{n}\otimes\boldsymbol{n} \\ \bar{\boldsymbol{E}}^{-1} = \dfrac{1}{\alpha_{\mathrm{t}}}(\boldsymbol{I} - \boldsymbol{n}\otimes\boldsymbol{n}) + \dfrac{1}{\alpha_{\mathrm{n}}}\boldsymbol{n}\otimes\boldsymbol{n} \\ \quad = \dfrac{1}{\alpha_{\mathrm{t}}}(\bar{\boldsymbol{e}}_1\otimes\bar{\boldsymbol{e}}_1 + \bar{\boldsymbol{e}}_2\otimes\bar{\boldsymbol{e}}_2) + \dfrac{1}{\alpha_{\mathrm{n}}}\boldsymbol{n}\otimes\boldsymbol{n} \end{cases} \tag{16}$$

where α_{n} and α_{t} denote the normal and tangential contact elastic moduli, respectively. Applying Eq. (16) to Eq. (15) yields

$$\begin{cases} \boldsymbol{f} = \alpha_{\mathrm{t}}\bar{\boldsymbol{u}}_{\mathrm{t}}^{\mathrm{e}} + \alpha_{\mathrm{n}}\bar{\boldsymbol{u}}_{\mathrm{n}}^{\mathrm{e}} \\ \bar{\boldsymbol{u}}^{\mathrm{e}} = \dfrac{1}{\alpha_{\mathrm{t}}}\boldsymbol{f}_{\mathrm{t}} + \dfrac{1}{\alpha_{\mathrm{n}}}\boldsymbol{f}_{\mathrm{n}} \end{cases} \tag{17}$$

The contact traction and the elastic sliding displacement are described in terms of their components with respect to the rectangular coordinate system as Eq. (18):

$$\begin{cases} \boldsymbol{f} = f_1\bar{\boldsymbol{e}}_1 + f_2\bar{\boldsymbol{e}}_2 + f_{\mathrm{n}}\boldsymbol{n} \\ \bar{\boldsymbol{u}}^{\mathrm{e}} = \bar{u}_1^{\mathrm{e}}\bar{\boldsymbol{e}}_1 + \bar{u}_2^{\mathrm{e}}\bar{\boldsymbol{e}}_2 + \bar{u}_{\mathrm{n}}^{\mathrm{e}}\boldsymbol{n} \end{cases} \tag{18}$$

The substitution of Eqs. (16) and (18) into Eq. (15) yields the matrix representation in Eq. (19):

$$\begin{Bmatrix} f_1 \\ f_2 \\ f_{\mathrm{n}} \end{Bmatrix} = \begin{bmatrix} \alpha_{\mathrm{t}} & 0 & 0 \\ 0 & \alpha_{\mathrm{t}} & 0 \\ 0 & 0 & \alpha_{\mathrm{n}} \end{bmatrix} \begin{Bmatrix} \bar{u}_1^{\mathrm{e}} \\ \bar{u}_2^{\mathrm{e}} \\ \bar{u}_{\mathrm{n}}^{\mathrm{e}} \end{Bmatrix} \tag{19}$$

and its inverse relation is

$$\begin{Bmatrix} \bar{u}_1^{\mathrm{e}} \\ \bar{u}_2^{\mathrm{e}} \\ \bar{u}_{\mathrm{n}}^{\mathrm{e}} \end{Bmatrix} = \begin{bmatrix} 1/\alpha_{\mathrm{t}} & 0 & 0 \\ 0 & 1/\alpha_{\mathrm{t}} & 0 \\ 0 & 0 & 1/\alpha_{\mathrm{n}} \end{bmatrix} \begin{Bmatrix} f_1 \\ f_2 \\ f_{\mathrm{n}} \end{Bmatrix}$$

where $\bar{\boldsymbol{e}}_1 \cdot \bar{\boldsymbol{e}}_2 = \bar{\boldsymbol{e}}_1 \cdot \boldsymbol{n} = \bar{\boldsymbol{e}}_2 \cdot \boldsymbol{n} = 0$.

It is noteworthy that the hyperelastic equation provides a one-to-one correspondence between the elastic sliding displacement $\bar{\boldsymbol{u}}^{\mathrm{e}}$ and the contact traction $\boldsymbol{f}$, from which one can calculate $\boldsymbol{f}$ directly by substituting $\bar{\boldsymbol{u}}^{\mathrm{e}}$. Hence, neither the rate equation of the hypoelastic law in terms of a co-rotational rate of $\boldsymbol{f}$ nor its time integration is required.

4 Elastoplastic sliding velocity

The subloading-friction model is formulated based on the concept of a subloading surface. The model is composed of the sliding-yield criterion, the hardening/softening rule of the friction coefficient, the evolution rule for the plastic sliding velocity, and a variable associated with the sliding-subloading surface.

4.1 Sliding normal-yield surface and sliding-subloading surface

Let us consider the sliding-yield surface defined by the following friction-yield function $f(\boldsymbol{f})$ with isotropic hardening/softening (Fig. 1):

$$f(\boldsymbol{f}) = \mu \tag{20}$$

which specifies the criterion of friction yielding, with the friction coefficient μ being the function describing the friction hardening/softening, i.e., the variation in the size of the sliding-yield surface. The friction-yield function $f(\boldsymbol{f})$ in terms of the contact traction $\boldsymbol{f}$ for the Coulomb friction law is expressed as

$$f(\boldsymbol{f}) = \frac{f_{\mathrm{t}}}{f_{\mathrm{n}}} \tag{21}$$

The variation in μ depending on the state of contact traction and/or the history of the sliding process is

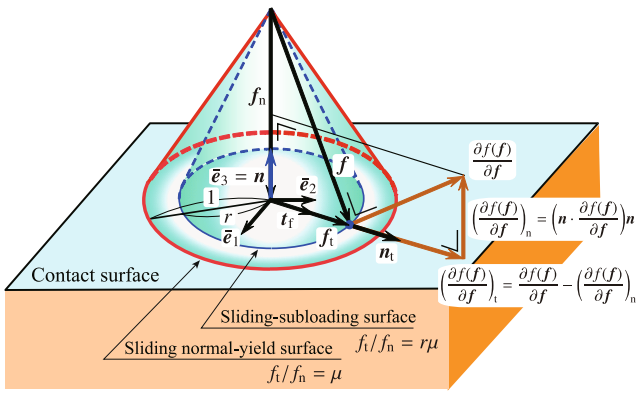

Fig. 1 Coulomb-type sliding normal-yield and sliding-subloading surfaces.

defined by the friction hardening/softening rule, which is described in Section 4.2. Next, we introduce the subloading surface concept: The plastic sliding velocity evolves as the magnitude of contact traction approaches the sliding-yield limit. Based on this notion, we introduce a sliding-subloading surface that has a shape and orientation similar to those of the sliding-yield surface and passes through the current contact traction. Hereinafter, the sliding-yield surface is renamed as the sliding normal-yield surface to distinguish it from the sliding-subloading surface. Furthermore, we introduce a scalar parameter, named the sliding normal-yield ratio, denoted by r ($0 \le r \le 1$), which defines the ratio of the size of the sliding-subloading surface to the size of the sliding normal-yield surface. It is vital to the subloading-friction model as it designates the approaching degree of contact traction to the sliding-normal yield surface. Subsequently, the sliding-subloading surface is represented as

$$f(\boldsymbol{f}) = r\mu \tag{22}$$

Figure 1 shows a schematic diagram of the sliding-subloading surface for the Coulomb friction law defined by Eq. (22) based on Eq. (21).

The time differentiation of Eq. (22) provides the consistency condition for the sliding-subloading surface, as Eq. (23):

$$\frac{\partial f(\boldsymbol{f})}{\partial \boldsymbol{f}} \cdot \dot{\boldsymbol{f}} = r\dot{\mu} + \dot{r}\mu \tag{23}$$

At this stage, we formulate the isotropic hardening/softening rule to define the friction coefficient μ and the evolution rule of the sliding normal-yield ratio r, which will be presented in Sections 4.2 and 4.3, respectively.

4.2 Friction hardening/softening rule for friction coefficient

The following can be inferred based on the experimental findings:

1) The friction coefficient μ transiently gains the maximum value of static friction, and then decreases to the minimum stationary value of kinetic friction. Subsequently, we assume that plastic sliding causes a decrease in the friction coefficient, namely, plastic softening, which corresponds to the transition from static friction to kinetic friction.

2) The friction coefficient gradually recovers its initial value at static friction during sliding suspension. Subsequently, we assume that the duration causes an increase in the friction coefficient, i.e., viscoplastic-like hardening.

Considering the above, we postulate the following isotropic hardening/softening function describing the variation in the friction coefficient μ [23, 27]:

$$\dot{\mu} = -\kappa\left(\mu - \mu_{\mathrm{k}}\right) \| \dot{\bar{\boldsymbol{u}}}^{\mathrm{p}} \| + \xi\left(\mu_{\mathrm{s}} - \mu\right) \tag{24}$$

or in the differential form:

$$\mathrm{d}\mu = \underbrace{-\kappa(\mu - \mu_{\mathrm{k}}) \| \mathrm{d}\bar{\boldsymbol{u}}^{\mathrm{p}} \|}_{\text{Negative}} + \underbrace{\xi(\mu_{\mathrm{s}} - \mu)\mathrm{d}t}_{\text{Positive}} \tag{25}$$

where μ_{s} and μ_{k} ($\mu_{\mathrm{k}} \le \mu \le \mu_{\mathrm{s}}$) are the material constants representing the maximum and minimum values of μ corresponding to static friction and kinetic friction, respectively. The constant κ specifies the rate of decrease in μ during the plastic sliding process. The constant ξ specifies the rate of recovery of μ for the suspension duration. The first and second terms in Eq. (24) and their differential counterparts in Eq. (25) are associated with the destruction and reconstruction, respectively, of the engagements of surface asperities. The variations in the sliding coefficient, based on Eq. (25), are shown in Fig. 2.

4.3 Evolution rule of sliding normal-yield ratio

Based on the abovementioned hypothesis regarding elastoplastic sliding, the evolution of the sliding normal-yield ratio r must fulfill the following conditions for $\dot{\bar{\boldsymbol{u}}}^{\mathrm{p}} \neq \boldsymbol{0}$:

$$\dot{r}\begin{cases} \to +\infty, & r \to +0 : \text{quasi-elastic sliding state} \\ > 0, & 0 < r < 1 : \text{sliding sub-yield state} \\ = 0, & r = 1 : \text{sliding normal-yield state} \\ < 0, & r > 1 : \text{sliding over normal-yield state} \end{cases} \tag{26}$$

Therefore, we apply the following evolution rule:

$$\dot{r} = \bar{U}(r) \| \dot{\bar{\boldsymbol{u}}}^{\mathrm{p}} \| \ (\dot{\bar{\boldsymbol{u}}}^{\mathrm{p}} \neq \boldsymbol{0}) \tag{27}$$

with $\bar{U}(r)$ being the monotonically decreasing function

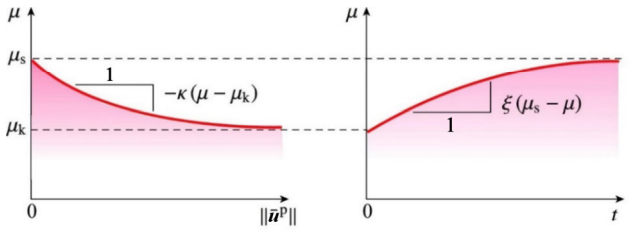

(a) Fast sliding process: $\|\mathrm{d}\bar{\boldsymbol{u}}^{\mathrm{p}}\| \gg \mathrm{d}t$ (b) Quasi-static sliding process: $\|\mathrm{d}\bar{\boldsymbol{u}}^{\mathrm{p}}\| \ll \mathrm{d}t$

Fig. 2 Variations in the friction coefficient.

of r, fulfilling the conditions:

$$\bar{U}(r)\begin{cases}\to+\infty, & r\to+0:\text{quasi-elastic sliding state}\\ >0, & 0<r<1:\text{sliding sub-yield state}\\ =0, & r=1:\text{sliding normal-yield state}\\ <0, & r>1:\text{sliding over normal-yield state}\end{cases} \tag{28}$$

Subsequently, we employ the following specific form of $\bar{U}(r)$:

$$\bar{U}(r)=\tilde{u}\cot\left(\frac{\pi}{2}r\right) \tag{29}$$

where $\tilde{u}$ is the evolution coefficient. The sliding normal-yield ratio r evolves along with the plastic sliding velocity, obeying the evolution rule shown in Eq. (27). Equation (29) implies that the increase in r with the progress of plastic sliding displacement becomes less significant as the value of $\tilde{u}$ decreases. Furthermore, it is noteworthy that the plastic sliding displacement required for a certain increase in r increases with r because of $\cot((\pi/2)r)$, and thus $\bar{U}(r)$ is the decreasing function of r.

Meanwhile, in the case of purely elastic sliding, the sliding normal-yield ratio r is calculated by substituting the contact traction at a current state obeying the elastic sliding constitutive relation, along with the current value of μ, into the equation of the sliding-subloading surface shown in Eq. (22), and then solving it for r.

According to Eq. (27) and using Eqs. $(28)_2$ and $(28)_3$, contact traction is automatically attracted onto the sliding normal-yield surface during plastic sliding. Meanwhile, contact traction is pulled back onto the sliding normal-yield surface when the contact traction exceeds the sliding normal-yield surface because $\dot{r}<0$ for $r>1$, based on Eqs. (27) and $(28)_4$. The characteristics of Eq. (28), as illustrated in Fig. 3, are advantageous in numerical calculations, as they effectively reduce the numerical errors in the incremental step analysis.

4.4 Plastic sliding velocity

The partial derivative of the sliding-yield function is expressed as

$$\begin{aligned}\frac{\partial f(\boldsymbol{f})}{\partial \boldsymbol{f}}&=\frac{\partial f(\boldsymbol{f})}{\partial \boldsymbol{f}_{\mathrm{t}}}\frac{\partial \boldsymbol{f}_{\mathrm{t}}}{\partial \boldsymbol{f}}+\frac{\partial f(\boldsymbol{f})}{\partial \boldsymbol{f}_{\mathrm{n}}}\frac{\partial \boldsymbol{f}_{\mathrm{n}}}{\partial \boldsymbol{f}}\\&=\frac{\partial f(\boldsymbol{f})}{\partial \boldsymbol{f}_{\mathrm{t}}}\left(\boldsymbol{I}-\boldsymbol{n}\otimes\boldsymbol{n}\right)+\frac{\partial f(\boldsymbol{f})}{\partial \boldsymbol{f}_{\mathrm{n}}}\boldsymbol{n}\otimes\boldsymbol{n}\end{aligned} \tag{30}$$

noting

$$\begin{cases}\dfrac{\partial \boldsymbol{f}_{\mathrm{n}}}{\partial \boldsymbol{f}}=\dfrac{\partial\left[(\boldsymbol{n}\otimes\boldsymbol{n})\boldsymbol{f}\right]}{\partial \boldsymbol{f}}=\boldsymbol{n}\otimes\boldsymbol{n}\\ \dfrac{\partial \boldsymbol{f}_{\mathrm{t}}}{\partial \boldsymbol{f}}=\dfrac{\partial\left[\left(\boldsymbol{I}-\boldsymbol{n}\otimes\boldsymbol{n}\right)\boldsymbol{f}\right]}{\partial \boldsymbol{f}}=\boldsymbol{I}-\boldsymbol{n}\otimes\boldsymbol{n}\end{cases} \tag{31}$$

Subsequently, based on Eq. (11),

$$\begin{cases}\dfrac{\partial \boldsymbol{f}_{\mathrm{n}}}{\partial \boldsymbol{f}}=\dfrac{\partial(-\boldsymbol{f}\cdot\boldsymbol{n})}{\partial \boldsymbol{f}}=-\boldsymbol{n}\boldsymbol{I}=-\boldsymbol{n}\\ \dfrac{\partial \boldsymbol{f}_{\mathrm{t}}}{\partial \boldsymbol{f}}=\dfrac{\partial\|\boldsymbol{f}_{\mathrm{t}}\|}{\partial \boldsymbol{f}}=\dfrac{\partial\|\boldsymbol{f}_{\mathrm{t}}\|}{\partial \boldsymbol{f}_{\mathrm{t}}}\dfrac{\partial \boldsymbol{f}_{\mathrm{t}}}{\partial \boldsymbol{f}}\\ \quad=\dfrac{\boldsymbol{f}_{\mathrm{t}}}{\|\boldsymbol{f}_{\mathrm{t}}\|}\dfrac{\partial\left[(\boldsymbol{I}-\boldsymbol{n}\otimes\boldsymbol{n})\boldsymbol{f}\right]}{\partial \boldsymbol{f}}=\dfrac{\boldsymbol{f}_{\mathrm{t}}}{\|\boldsymbol{f}_{\mathrm{t}}\|}(\boldsymbol{I}-\boldsymbol{n}\otimes\boldsymbol{n})=\boldsymbol{t}_{\mathrm{f}}\end{cases} \tag{32}$$

Substituting Eqs. (24) and (27) into Eq. (23) yields

$$\begin{aligned}\frac{\partial f(\boldsymbol{f})}{\partial \boldsymbol{f}}\cdot\dot{\boldsymbol{f}}=r\Big[&-\kappa\left(\mu-\mu_{\mathrm{k}}\right)\|\dot{\bar{\boldsymbol{u}}}^{\mathrm{p}}\|+\xi\left(\mu_{\mathrm{s}}-\mu\right)\Big]\\&+\bar{U}(r)\|\dot{\bar{\boldsymbol{u}}}^{\mathrm{p}}\|\mu\end{aligned} \tag{33}$$

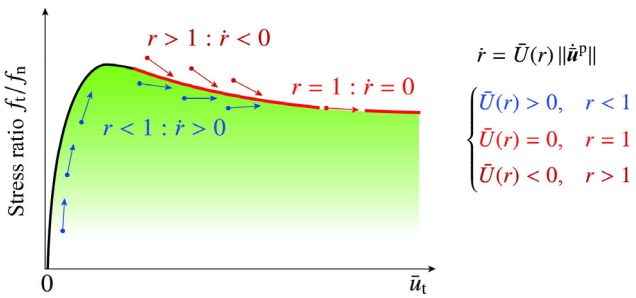

Fig. 3 Contact traction controlling feature in the evolution rule of r. Contact traction is automatically attracted to sliding normal-yield surface during plastic sliding.

Next, we assume that the direction of the plastic sliding velocity is tangential to the contact surface, and further assume that the plastic sliding velocity evolves in the direction of outward normal to the curve generated by the intersection of the sliding-subloading surface and the constant normal traction plane defined by $f_{\mathrm{n}} = \text{constant}$, which results in the tangential associated flow rule (Fig. 1), as Eq. (34):

$$\dot{\bar{\boldsymbol{u}}}^{\mathrm{p}} = \dot{\bar{\lambda}}\,\boldsymbol{n}_{\mathrm{t}} \quad (\dot{\bar{\lambda}} = \| \dot{\bar{\boldsymbol{u}}}^{\mathrm{p}} \| \geq 0,\ \boldsymbol{n}\cdot\dot{\bar{\boldsymbol{u}}}^{\mathrm{p}} = 0) \tag{34}$$

where

$$\boldsymbol{n}_{\mathrm{t}} \equiv \left(\frac{\partial f(\boldsymbol{f})}{\partial \boldsymbol{f}}\right)_{\mathrm{t}} \Bigg/ \left\| \left(\frac{\partial f(\boldsymbol{f})}{\partial \boldsymbol{f}}\right)_{\mathrm{t}} \right\| \quad (\| \boldsymbol{n}_{\mathrm{t}} \| = 1,\ \boldsymbol{n}\cdot\boldsymbol{n}_{\mathrm{t}} = 0) \tag{35}$$

and

$$\left(\frac{\partial f(\boldsymbol{f})}{\partial \boldsymbol{f}}\right)_{\mathrm{t}} \equiv \frac{\partial f(\boldsymbol{f})}{\partial \boldsymbol{f}} - \left(\boldsymbol{n}\cdot\frac{\partial f(\boldsymbol{f})}{\partial \boldsymbol{f}}\right)\boldsymbol{n} = \left(\boldsymbol{I} - \boldsymbol{n}\otimes\boldsymbol{n}\right)\frac{\partial f(\boldsymbol{f})}{\partial \boldsymbol{f}} \tag{36}$$

where $\dot{\bar{\lambda}}$ and $\boldsymbol{n}_{\mathrm{t}}$ are the magnitude and direction of the plastic sliding velocity, respectively.

Substituting Eq. (34) into Eq. (33) yields

$$\frac{\partial f(\boldsymbol{f})}{\partial \boldsymbol{f}}\cdot\dot{\boldsymbol{f}} = \dot{\bar{\lambda}} m^{\mathrm{p}} + m^{\mathrm{c}} \tag{37}$$

where

$$\begin{cases} m^{\mathrm{p}} \equiv -\kappa(\mu - \mu_{\mathrm{k}})r + \bar{U}(r)\,\mu \\ m^{\mathrm{c}} \equiv \xi(\mu_{\mathrm{s}} - \mu)r \quad (\ m^{\mathrm{c}} \geq 0) \end{cases} \tag{38}$$

which are associated with the plastic and the creep sliding velocities, respectively.

Based on Eqs. (34) and (37), we obtain

$$\begin{cases} \dot{\bar{\lambda}} = \dfrac{\dfrac{\partial f(\boldsymbol{f})}{\partial \boldsymbol{f}}\cdot\dot{\boldsymbol{f}} - m^{\mathrm{c}}}{m^{\mathrm{p}}} \\ \dot{\bar{\boldsymbol{u}}}^{\mathrm{p}} = \dfrac{\dfrac{\partial f(\boldsymbol{f})}{\partial \boldsymbol{f}}\cdot\dot{\boldsymbol{f}} - m^{\mathrm{c}}}{m^{\mathrm{p}}}\boldsymbol{n}_{\mathrm{t}} \end{cases} \tag{39}$$

By substituting the rate form of Eq. $(15)_2$ and Eq. $(39)_2$ into the rate form of Eq. (4), the sliding velocity is expressed as

$$\dot{\bar{\boldsymbol{u}}} = \bar{\boldsymbol{E}}^{-1}\dot{\boldsymbol{f}} + \frac{\dfrac{\partial f(\boldsymbol{f})}{\partial \boldsymbol{f}}\cdot\dot{\boldsymbol{f}} - m^{\mathrm{c}}}{m^{\mathrm{p}}}\boldsymbol{n}_{\mathrm{t}} \tag{40}$$

Subsequently, based on Eq. (40),

$$\frac{\partial f(\boldsymbol{f})}{\partial \boldsymbol{f}}\cdot\bar{\boldsymbol{E}}\,\dot{\bar{\boldsymbol{u}}} = \frac{\partial f(\boldsymbol{f})}{\partial \boldsymbol{f}}\cdot\dot{\boldsymbol{f}} + \frac{\dfrac{\partial f(\boldsymbol{f})}{\partial \boldsymbol{f}}\cdot\dot{\boldsymbol{f}} - m^{\mathrm{c}}}{m^{\mathrm{p}}}\frac{\partial f(\boldsymbol{f})}{\partial \boldsymbol{f}}\cdot\bar{\boldsymbol{E}}\,\boldsymbol{n}_{\mathrm{t}}$$

which results in

$$\begin{aligned} \frac{\partial f(\boldsymbol{f})}{\partial \boldsymbol{f}}\cdot\bar{\boldsymbol{E}}\,\dot{\bar{\boldsymbol{u}}} = {} & m^{\mathrm{p}}\frac{\dfrac{\partial f(\boldsymbol{f})}{\partial \boldsymbol{f}}\cdot\dot{\boldsymbol{f}} - m^{\mathrm{c}}}{m^{\mathrm{p}}} + m^{\mathrm{c}} \\ & + \frac{\dfrac{\partial f(\boldsymbol{f})}{\partial \boldsymbol{f}}\cdot\dot{\boldsymbol{f}} - m^{\mathrm{c}}}{m^{\mathrm{p}}}\frac{\partial f(\boldsymbol{f})}{\partial \boldsymbol{f}}\cdot\bar{\boldsymbol{E}}\,\boldsymbol{n}_{\mathrm{t}} \end{aligned}$$

i.e.,

$$\frac{\partial f(\boldsymbol{f})}{\partial \boldsymbol{f}}\cdot\bar{\boldsymbol{E}}\,\dot{\bar{\boldsymbol{u}}} = \left(m^{\mathrm{p}} + \frac{\partial f(\boldsymbol{f})}{\partial \boldsymbol{f}}\cdot\bar{\boldsymbol{E}}\,\boldsymbol{n}_{\mathrm{t}}\right)\dot{\bar{\lambda}} + m^{\mathrm{c}}$$

from which the plastic multiplier in terms of the sliding velocity, denoted by the symbol $\dot{\bar{\Lambda}}$, is expressed as

$$\begin{cases} \dot{\bar{\Lambda}} = \dfrac{\dfrac{\partial f(\boldsymbol{f})}{\partial \boldsymbol{f}}\cdot\bar{\boldsymbol{E}}\,\dot{\bar{\boldsymbol{u}}} - m^{\mathrm{c}}}{m^{\mathrm{p}} + \dfrac{\partial f(\boldsymbol{f})}{\partial \boldsymbol{f}}\cdot\bar{\boldsymbol{E}}\,\boldsymbol{n}_{\mathrm{t}}} \\ \dot{\bar{\boldsymbol{u}}}^{\mathrm{p}} = \dfrac{\dfrac{\partial f(\boldsymbol{f})}{\partial \boldsymbol{f}}\cdot\bar{\boldsymbol{E}}\,\dot{\bar{\boldsymbol{u}}} - m^{\mathrm{c}}}{m^{\mathrm{p}} + \dfrac{\partial f(\boldsymbol{f})}{\partial \boldsymbol{f}}\cdot\bar{\boldsymbol{E}}\,\boldsymbol{n}_{\mathrm{t}}}\boldsymbol{n}_{\mathrm{t}} \end{cases} \tag{41}$$

By substituting the rate form of Eq. (4) with Eq. $(41)_2$ into the rate form of Eq. $(15)_1$, we obtain the inverse relation of Eq. (40) as Eq. (42):

$$\dot{\boldsymbol{f}} = \left(\bar{\boldsymbol{E}} - \frac{\bar{\boldsymbol{E}}\,\boldsymbol{n}_{\mathrm{t}}\otimes\dfrac{\partial f(\boldsymbol{f})}{\partial \boldsymbol{f}}\bar{\boldsymbol{E}}}{m^{\mathrm{p}} + \dfrac{\partial f(\boldsymbol{f})}{\partial \boldsymbol{f}}\cdot\bar{\boldsymbol{E}}\,\boldsymbol{n}_{\mathrm{t}}}\right)\dot{\bar{\boldsymbol{u}}} + \frac{m^{\mathrm{c}}}{m^{\mathrm{p}} + \dfrac{\partial f(\boldsymbol{f})}{\partial \boldsymbol{f}}\cdot\bar{\boldsymbol{E}}\,\boldsymbol{n}_{\mathrm{t}}}\bar{\boldsymbol{E}}\,\boldsymbol{n}_{\mathrm{t}} \tag{42}$$

The contact traction $\boldsymbol{f}$ can be calculated using the time integration of Eq. (42). Alternatively, it can be

calculated directly by substituting the elastic sliding displacement $\bar{\boldsymbol{u}}^{\mathrm{e}}$ into the hyperelastic equation, where $\bar{\boldsymbol{u}}^{\mathrm{e}}$ is obtained by subtracting the plastic sliding displacement vector $\bar{\boldsymbol{u}}^{\mathrm{p}}$ from the sliding displacement vector $\bar{\boldsymbol{u}}$. The loading criterion for the plastic sliding rate is expressed as

$$\begin{cases} \dot{\bar{\boldsymbol{u}}}^{\mathrm{p}} \neq \boldsymbol{0}, & \dot{\bar{\Lambda}} > 0 \\ \dot{\bar{\boldsymbol{u}}}^{\mathrm{p}} = \boldsymbol{0}, & \text{others} \end{cases} \tag{43}$$

4.5 Isotropic sliding-yield surface

The traction function for the isotropic sliding-yield surface is expressed as

$$f(\boldsymbol{f}) = f(f_{\mathrm{t}}, f_{\mathrm{n}}) \tag{44}$$

for which the following partial derivatives hold with the reference to Eq. (32):

$$\begin{aligned} \frac{\partial f(\boldsymbol{f})}{\partial \boldsymbol{f}} &= \frac{\partial f(f_{\mathrm{t}}, f_{\mathrm{n}})}{\partial \boldsymbol{f}} \\ &= \frac{\partial f(f_{\mathrm{t}}, f_{\mathrm{n}})}{\partial f_{\mathrm{n}}} \frac{\partial f_{\mathrm{n}}}{\partial \boldsymbol{f}} + \frac{\partial f(f_{\mathrm{t}}, f_{\mathrm{n}})}{\partial f_{t}} \frac{\partial f_{\mathrm{t}}}{\partial \boldsymbol{f}} \\ &= -\frac{\partial f(f_{\mathrm{t}}, f_{\mathrm{n}})}{\partial f_{\mathrm{n}}} \boldsymbol{n} + \frac{\partial f(f_{\mathrm{t}}, f_{\mathrm{n}})}{\partial f_{\mathrm{t}}} \boldsymbol{t}_{\mathrm{f}} \end{aligned} \tag{45}$$

Subsequently, substituting Eq. (45) into Eqs. (11) and (35) yields

$$\boldsymbol{n}_{\mathrm{t}} = \boldsymbol{t}_{\mathrm{f}} \tag{46}$$

Equation (46) confirms that the direction of the plastic sliding velocity coincides with the tangential direction of the traction.

Next, we adopt the following Coulomb-type sliding yield function as a specific form of $f(\boldsymbol{f})$ in Eq. (44):

$$f(\boldsymbol{f}) = \frac{f_{\mathrm{t}}}{f_{\mathrm{n}}} \tag{47}$$

Subsequently, based on Eqs. (45)–(47),

$$\begin{cases} \dfrac{\partial f(\boldsymbol{f})}{\partial f_{\mathrm{n}}} = -\dfrac{f_{\mathrm{t}}}{f_{\mathrm{n}}^2} \\ \dfrac{\partial f(\boldsymbol{f})}{\partial f_{\mathrm{t}}} = \dfrac{1}{f_{\mathrm{n}}} \end{cases} \tag{48}$$

and thus

$$\frac{\partial f(\boldsymbol{f})}{\partial \boldsymbol{f}} = \frac{1}{f_{\mathrm{n}}} \left(\boldsymbol{t}_{\mathrm{f}} + \frac{f_{\mathrm{t}}}{f_{\mathrm{n}}} \boldsymbol{n} \right) \tag{49}$$

Using Eq. (16) and $\boldsymbol{n} \cdot \boldsymbol{t}_{\mathrm{f}} = 0$, we obtain

$$\bar{\boldsymbol{E}} \boldsymbol{n}_{\mathrm{t}} = \bar{\boldsymbol{E}} \boldsymbol{t}_{\mathrm{f}} = \alpha_{\mathrm{t}} \boldsymbol{t}_{\mathrm{f}} \tag{50}$$

$$\begin{aligned} \bar{\boldsymbol{E}} \frac{\partial f(\boldsymbol{f})}{\partial \boldsymbol{f}} &= \left[\alpha_{\mathrm{t}} \left(\boldsymbol{I} - \boldsymbol{n} \otimes \boldsymbol{n} \right) + \alpha_{\mathrm{n}} \boldsymbol{n} \otimes \boldsymbol{n} \right] \frac{1}{f_{\mathrm{n}}} \left(\boldsymbol{t}_{\mathrm{f}} + \frac{f_{\mathrm{t}}}{f_{\mathrm{n}}} \boldsymbol{n} \right) \\ &= \frac{1}{f_{\mathrm{n}}} \left(\alpha_{\mathrm{t}} \boldsymbol{t}_{\mathrm{f}} + \alpha_{\mathrm{n}} \frac{f_{\mathrm{t}}}{f_{\mathrm{n}}} \boldsymbol{n} \right) \end{aligned} \tag{51}$$

$$\frac{\partial f(\boldsymbol{f})}{\partial \boldsymbol{f}} \cdot \bar{\boldsymbol{E}} \boldsymbol{t}_{\mathrm{f}} = \frac{1}{f_{\mathrm{n}}} \left(\boldsymbol{t}_{\mathrm{f}} + \frac{f_{\mathrm{t}}}{f_{\mathrm{n}}} \boldsymbol{n} \right) \cdot \alpha_{\mathrm{t}} \boldsymbol{t}_{\mathrm{f}} = \frac{\alpha_{\mathrm{t}}}{f_{\mathrm{n}}} \tag{52}$$

$$\begin{aligned} \frac{\partial f(\boldsymbol{f})}{\partial \boldsymbol{f}} \cdot \bar{\boldsymbol{E}} \dot{\bar{\boldsymbol{u}}} &= \frac{1}{f_{\mathrm{n}}} \left(\boldsymbol{t}_{\mathrm{f}} + \frac{f_{\mathrm{t}}}{f_{\mathrm{n}}} \boldsymbol{n} \right) \cdot \left[\alpha_{\mathrm{t}} \left(\boldsymbol{I} - \boldsymbol{n} \otimes \boldsymbol{n} \right) + \alpha_{\mathrm{n}} \boldsymbol{n} \otimes \boldsymbol{n} \right] \dot{\bar{\boldsymbol{u}}} \\ &= \frac{1}{f_{\mathrm{n}}} \left(\alpha_{\mathrm{t}} \boldsymbol{t}_{\mathrm{f}} + \alpha_{\mathrm{n}} \frac{f_{\mathrm{t}}}{f_{\mathrm{n}}} \boldsymbol{n} \right) \cdot \dot{\bar{\boldsymbol{u}}} \end{aligned} \tag{53}$$

By substituting Eqs. (50)–(53), Eqs. (40) and (42) are reduced to

$$\begin{aligned} \dot{\bar{\boldsymbol{u}}} = &\left[\frac{1}{\alpha_{\mathrm{t}}} \left(\boldsymbol{I} - \boldsymbol{n} \otimes \boldsymbol{n} \right) + \frac{1}{\alpha_{\mathrm{n}}} \boldsymbol{n} \otimes \boldsymbol{n} \right] \dot{\boldsymbol{f}} \\ &+ \frac{\dfrac{1}{f_{\mathrm{n}}} \left(\boldsymbol{t}_{\mathrm{f}} + \dfrac{f_{\mathrm{t}}}{f_{\mathrm{n}}} \boldsymbol{n} \right) \cdot \dot{\boldsymbol{f}} - m^{\mathrm{c}}}{m^{\mathrm{p}}} \boldsymbol{t}_{\mathrm{f}} \end{aligned} \tag{54}$$

and

$$\begin{aligned} \dot{\boldsymbol{f}} = &\left[\alpha_{\mathrm{t}} \left(\boldsymbol{I} - \boldsymbol{n} \otimes \boldsymbol{n} \right) + \alpha_{\mathrm{n}} \boldsymbol{n} \otimes \boldsymbol{n} \right] \\ &\times \left[\dot{\bar{\boldsymbol{u}}} - \left\langle \frac{\dfrac{1}{f_{\mathrm{n}}} \left(\alpha_{\mathrm{t}} \boldsymbol{t}_{\mathrm{f}} + \alpha_{\mathrm{n}} \dfrac{f_{\mathrm{t}}}{f_{\mathrm{n}}} \boldsymbol{n} \right) \cdot \dot{\bar{\boldsymbol{u}}} - m^{\mathrm{c}}}{m^{\mathrm{p}} + \dfrac{\alpha_{\mathrm{t}}}{f_{\mathrm{n}}}} \right\rangle \boldsymbol{t}_{\mathrm{f}} \right] \end{aligned} \tag{55}$$

where $\langle \cdot \rangle$ is the Macaulay's bracket, i.e., $\langle s \rangle$ for $s \geq 0$ and $s = 0$ for $s < 0$, where s is a scalar argument.

In the coordinate system with base $(\bar{\boldsymbol{e}}_1, \bar{\boldsymbol{e}}_2, \boldsymbol{n})$, by considering:

$$\begin{aligned} \boldsymbol{I} - \boldsymbol{n} \otimes \boldsymbol{n} &= (\bar{\boldsymbol{e}}_1 \otimes \bar{\boldsymbol{e}}_1 + \bar{\boldsymbol{e}}_2 \otimes \bar{\boldsymbol{e}}_2 + \boldsymbol{n} \otimes \boldsymbol{n}) - \boldsymbol{n} \otimes \boldsymbol{n} \\ &= \bar{\boldsymbol{e}}_1 \otimes \bar{\boldsymbol{e}}_1 + \bar{\boldsymbol{e}}_2 \otimes \bar{\boldsymbol{e}}_2 \end{aligned} \tag{56}$$

we have

$$\boldsymbol{t}_{\mathrm{f}} = t_{\mathrm{f}1} \bar{\boldsymbol{e}}_1 + t_{\mathrm{f}2} \bar{\boldsymbol{e}}_2 \tag{57}$$

where

$$t_{\mathrm{f}1}=\frac{f_1}{\|\boldsymbol{f}_{\mathrm{t}}\|}=\frac{f_1}{\sqrt{f_1^2+f_2^2}},\ t_{\mathrm{f}2}=\frac{f_2}{\|\boldsymbol{f}_{\mathrm{t}}\|}=\frac{f_2}{\sqrt{f_1^2+f_2^2}}$$

By substituting Eqs. (56) and (57), Eq. (55) is reduced to

$$\begin{aligned}\dot{\boldsymbol{f}}=&\left[\alpha_{\mathrm{t}}\left(\bar{\boldsymbol{e}}_1\otimes\bar{\boldsymbol{e}}_1+\bar{\boldsymbol{e}}_2\otimes\bar{\boldsymbol{e}}_2\right)+\alpha_{\mathrm{n}}\boldsymbol{n}\otimes\boldsymbol{n}\right]\dot{\bar{\boldsymbol{u}}}\\&-\alpha_{\mathrm{t}}(t_{\mathrm{f}1}\bar{\boldsymbol{e}}_1+t_{\mathrm{f}2}\bar{\boldsymbol{e}}_2)\\&\times\left\langle\frac{\dfrac{1}{f_{\mathrm{n}}}\left(\alpha_{\mathrm{t}}\left(t_{\mathrm{f}1}\bar{\boldsymbol{e}}_1+t_{\mathrm{f}2}\bar{\boldsymbol{e}}_2\right)+\alpha_{\mathrm{n}}\dfrac{f_{\mathrm{t}}}{f_{\mathrm{n}}}\boldsymbol{n}\right)\cdot\dot{\bar{\boldsymbol{u}}}-m^{\mathrm{c}}}{m^{\mathrm{p}}+\dfrac{\alpha_{\mathrm{t}}}{f_{\mathrm{n}}}}\right\rangle\end{aligned}\tag{58}$$

4.6 Linear sliding behavior

Next, we examine the linear sliding phenomenon under a constant normal traction with a fixed direction of tangential contact traction, in which the following relations hold:

$$\begin{cases}\boldsymbol{f}_{\mathrm{n}}=\text{const.},\ \boldsymbol{t}_{\mathrm{f}}=\text{const.}\\ \dot{\boldsymbol{f}}_{\mathrm{n}}=\boldsymbol{0},\ \dot{\boldsymbol{f}}=\dot{\boldsymbol{f}}_{\mathrm{t}}=\dot{f}_{\mathrm{t}}\boldsymbol{t}_{\mathrm{f}}\\ \dot{\bar{\boldsymbol{u}}}_{\mathrm{n}}=\dot{\bar{\boldsymbol{u}}}_{\mathrm{n}}^{\mathrm{e}}=\dot{\bar{\boldsymbol{u}}}_{\mathrm{n}}^{\mathrm{p}}=\boldsymbol{0},\ \dot{\bar{\boldsymbol{u}}}^{\mathrm{e}}=\dot{\bar{u}}_{\mathrm{t}}^{\mathrm{e}}\boldsymbol{t}_{\mathrm{f}},\ \dot{\bar{\boldsymbol{u}}}=\dot{\bar{u}}_{\mathrm{t}}\boldsymbol{t}_{\mathrm{f}}\end{cases}\tag{59}$$

Equations (54) and (55) are reduced to the following relations in one-dimensional sliding under the condition shown in Eq. (59), using notations $\dot{f}_{\mathrm{t}1}\to\dot{f}_{\mathrm{t}}$, $\dot{\bar{u}}_{\mathrm{t}1}\to\dot{\bar{u}}_{\mathrm{t}}$ ($\dot{f}_{\mathrm{t}2}=0$, $\dot{f}_{\mathrm{n}}=0$, $\dot{\bar{u}}_{\mathrm{t}2}=0$, and $\dot{\bar{u}}_{\mathrm{n}}=0$) as well as Eq. (38):

$$\dot{\bar{u}}_{\mathrm{t}}=\frac{1}{\alpha_{\mathrm{t}}}\dot{f}_{\mathrm{t}}+\frac{\dfrac{f_{\mathrm{t}}}{f_{\mathrm{n}}}-m^{\mathrm{c}}}{m^{\mathrm{p}}}=\frac{1}{\alpha_{\mathrm{t}}}\dot{f}_{\mathrm{t}}+\frac{\dfrac{f_{\mathrm{t}}}{f_{\mathrm{n}}}-\xi(\mu_{\mathrm{s}}-\mu)r}{-\kappa(\mu-\mu_{\mathrm{k}})r+\bar{U}(r)\mu}\tag{60}$$

where

$$\begin{aligned}\dot{f}_{\mathrm{t}}&=\alpha_{\mathrm{t}}\dot{\bar{u}}_{\mathrm{t}}-\alpha_{\mathrm{t}}\left\langle\frac{\dfrac{\alpha_{\mathrm{t}}}{f_{\mathrm{n}}}\dot{\bar{u}}_{\mathrm{t}}-m^{\mathrm{c}}}{m^{\mathrm{p}}+\dfrac{\alpha_{\mathrm{t}}}{f_{\mathrm{n}}}}\right\rangle\\&=\alpha_{\mathrm{t}}\dot{\bar{u}}_{\mathrm{t}}-\alpha_{\mathrm{t}}\left\langle\frac{\dfrac{\alpha_{\mathrm{t}}}{f_{\mathrm{n}}}\dot{\bar{u}}_{\mathrm{t}}-\xi\left(\mu_{\mathrm{s}}-\mu\right)r}{-\kappa\left(\mu-\mu_{\mathrm{k}}\right)r+\bar{U}(r)\mu+\dfrac{\alpha_{\mathrm{t}}}{f_{\mathrm{n}}}}\right\rangle\end{aligned}\tag{61}$$

5 Application to description of soil–metal friction

The applicability of the subloading-friction model for describing the soil–metal friction behavior is examined in this section. All the test data were one-dimensional, i.e., linear sliding, and they included the data from monotonic and cyclic sliding tests. Seven material constants, i.e., μ_{s}, μ_{k}, κ, ξ, $\tilde{u}$, α_{n}, and α_{t}, and the initial value of the friction coefficient, denoted by μ_0, were included in the present subloading-friction model. The initial friction coefficient was set as the static friction coefficient, i.e., $\mu_0=\mu_{\mathrm{s}}$, in all simulations.

The material parameters used in the present model were determined as follows:

1) The normal and tangential contact elastic moduli α_{n} and α_{t}, respectively, may be sufficiently large because they are relevant to the surface asperities of the contact interface. However, α_{n} and α_{t} do not significantly affect the contact stress vs. sliding displacement relationship provided that their values are sufficiently large. Therefore, a sufficiently large value can be set provided that it allows analysis to be performed stably.

2) The static and kinetic friction coefficients μ_{s} and μ_k ($\mu_k\le\mu_{\mathrm{s}}$) were determined, respectively, by the peak and bottom values of the ratio of the tangential contact stress to the normal contact stress. Therefore, these values can be determined directly from the experimental data.

3) The material constants κ and ξ were determined to reproduce the decrease in the friction coefficient due to plastic sliding and the recovery rate of the friction coefficient due to the pause of sliding. They interact mutually in the contact stress vs. sliding displacement relationship. If the experimental data of sufficiently fast and slow slidings are provided, and then the values of κ and ξ can be determined independently.

4) The material constant $\tilde{u}$ is determined to reproduce the smooth transition from the elastic to plastic state.

These material constants are independent of each other in terms of their physical meanings; therefore, they can be determined definitely, although the model simulation of the contact stress vs. sliding displacement relationship involves their combination.

5.1 Monotonic sliding behavior

First, we examine the simulation of the monotonic sliding behavior by comparing it with the test data measured by Uesugi and Kishida [47] using a direct shear apparatus. Dry Toyoura sand with D_{50} = 0.18 mm (average diameter) was used as the soil specimen. Low-carbon structural steel (American Society for Testing and Materials (ASTM) Specification for Structural Steel A36) plates were used for the metal specimens with three levels of roughness, i.e., $R_{max} = 0.6$ μm (smooth), $R_{max} = 6.8$ μm (medium), and $R_{max} = 9.8$ μm (rough). Here, R_{max} designates the relative height between the highest peak and the lowest valley along a surface profile over the gauge length [48]. A gauge length $L = 0.2$ mm was used to measure the surface roughness, considering the average diameter of the Toyoura sand (≃ 200 μm). The normal contact stress was 78.4 kPa. The model simulation is shown in Fig. 4, and its material parameters are listed in Table 1.

Next, the simulation of the test result for the monotonic sliding behavior measured by Yoshimi and Kishida [68] using a ring torsional shear apparatus is shown in Fig. 5. Tone River sand with a mean grain size of 0.27 mm (the relative density $D_r = 60\%$) was used as the soil specimen. The metal specimen was the same steel presented in Fig. 4. The surface roughness index of steel was $R_{max} = 3.3$–3.6 μm (the gauge length $L = 0.25$ mm). The normal contact stress was 105 kPa. The material parameters used are listed in Table 2.

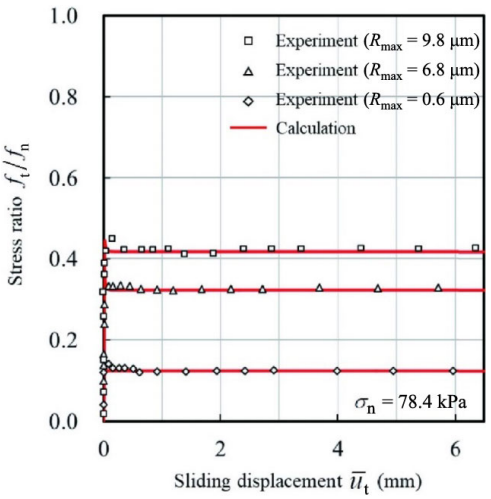

Fig. 4 Comparison with the test data by Uesugi and Kishida [47] in monotonic sliding between sand and steel in direct shear test.

Table 1 Material parameters used in the simulation of the monotonic sliding in direct shear test [47] shown in Fig. 4.

R_{max}	0.6 μm	6.8 μm	9.8 μm
Parameter		Value	
μ_s	0.20	0.37	0.45
μ_k	0.10	0.30	0.40
κ(mm^{-1})	100	33	25
ξ(s^{-1})	0.050	0.027	0.022
$\tilde{u}$(mm^{-1})	200	3,000	3,000
α_n(kN·mm^{-3})	2,000	2,000	2,000
α_t(kN·mm^{-3})	2,000	2,000	2,000

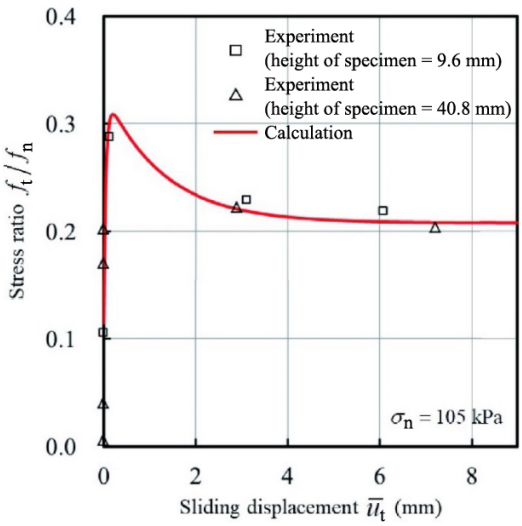

Fig. 5 Comparison with the test data by Yoshimi and Kishida [68] in monotonic sliding between sand and steel in ring torsional shear test.

Table 2 Material parameters used in the simulation of the monotonic sliding in ring torsional shear test [68] shown in Fig. 5.

Parameter	Value
μ_s	0.33
μ_k	0.17
κ(mm^{-1})	0.59
ξ(s^{-1})	0.0030
$\tilde{u}$(mm^{-1})	12
α_n(kN·mm^{-3})	10,000
α_t(kN·mm^{-3})	10,000

5.2 Cyclic sliding behavior

The simulation of the cyclic sliding behavior was analyzed by comparing the result with the test data obtained by Uesugi et al. [50]. Toyoura sand with $D_{50} = 0.18$ mm and steel plate A36 were used. The surface roughness index of steel was $R_{max} = 3.3$–3.6 μm (the gauge length $L = 0.25$ mm) for pulsating sliding.

The surface roughness index of the steel was $R_{max} = 28$ μm (the gauge length $L = 0.2$ mm) for two-way sliding. The normal contact stress was 98 kPa. The model simulations for the pulsating and two-way cyclic sliding are shown in Figs. 6 and 7, respectively. The material parameters used in these analyses are listed in Tables 3 and 4.

Precise simulations were performed for all the test data obtained from the monotonic and cyclic (pulsating and two-way) sliding behaviors up to the finite sliding displacements between sands and metals using the subloading-friction model.

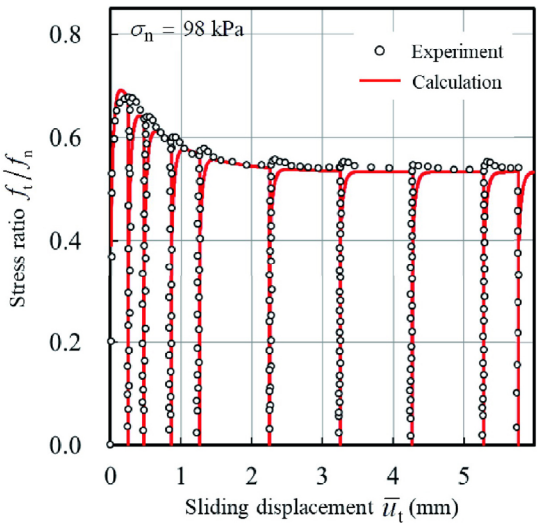

Fig. 6 Comparison with the test data by Uesugi et al. [50] in one-way cyclic (pulsating) sliding between sand and steel.

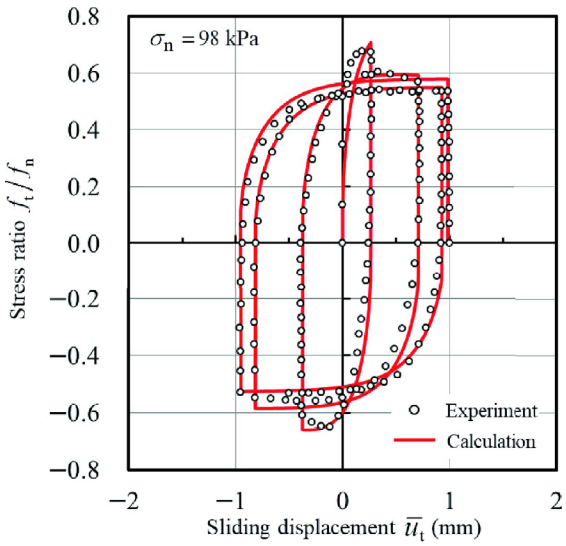

Fig. 7 Comparison with the test data by Uesugi et al. [50] in two-way cyclic siding between sand and steel.

Table 3 Material parameters used in the simulation of the one-way cyclic (pulsating) sliding test [50] shown in Fig. 6.

Parameter	Value
μ_s	0.74
μ_k	0.52
$\kappa(\mathrm{mm}^{-1})$	1.3
$\xi(\mathrm{s}^{-1})$	0.0014
$\tilde{u}(\mathrm{mm}^{-1})$	15
$\alpha_n(\mathrm{kN{\cdot}mm}^{-3})$	5,000
$\alpha_t(\mathrm{kN{\cdot}mm}^{-3})$	5,000

Table 4 Material parameters used in the simulation of the two-way cyclic sliding test [50] shown in Fig. 7.

Parameter	Value
μ_s	1.1
μ_k	0.50
$\kappa(\mathrm{mm}^{-1})$	1.2
$\xi(\mathrm{s}^{-1})$	0.00091
$\tilde{u}(\mathrm{mm}^{-1})$	2.0
$\alpha_n(\mathrm{kN{\cdot}mm}^{-3})$	50,000
$\alpha_t(\mathrm{kN{\cdot}mm}^{-3})$	50,000

6 Conclusions

In this study, we verified the applicability of the subloading-friction model for describing the frictional sliding behavior on soil–metal interface by comparing its results with the experimental data of monotonic and cyclic sliding behaviors under various conditions. The main features of the proposed model are summarized as follows:

1) The irreversible sliding caused by the change in contact traction below the sliding yield traction was successfully described via the subloading surface concept, i.e., the irreversible sliding rate develops gradually as the contact traction approaches the sliding-yield surface.

2) The smooth transition from static friction to kinetic friction was described.

3) The recovery of the friction coefficient after the sliding suspended, or the sliding velocity decreased to an extremely slow velocity.

4) Not only the monotonic sliding but also the cyclic sliding behavior can be described.

5) The finite sliding behaviors involving large

nonlinear sliding displacements and rotations of the soil–metal interface can be described appropriately.

The validity of the subloading-friction model for describing the friction behavior between various sands and metals was demonstrated in this study based on the simulation of the test results under monotonic and cyclic sliding displacements. Consequently, the subloading-friction model would contribute to the prediction of the frictional sliding behavior occurring in various geotechnical structures, e.g., foundation piles, retaining walls, and construction machinery.

Acknowledgements

This study was partially supported by Japan Society for the Promotion of Science (JSPS), KAKENHI, Grant-in-Aid for Scientific Research (C), Grant No. JP19K04566 for Yuki YAMAKAWA.

References

[1] Dokos S J. Sliding friction under extreme pressures–I. *J Appl Mech Trans ASME* **68**: A148–A156 (1946)

[2] Rabinowicz E. The nature of the static and kinetic coefficients of friction. *J Appl Phys* **22**(11): 1373–1379 (1951)

[3] Howe P G, Benton D P, Puddington I E. London–van der Waals attractive forces between glass surfaces. *Can J Chem* **33**(9): 1375–1383 (1955)

[4] Derjaguin B V, Push V E, Tolstoi D M. A theory of stick-slipping of solids. In: Proceedings of the Lubrication and Wear (Inst Mech Eng), London, 1957: 257–268.

[5] Rabinowicz E. The intrinsic variables affecting the stick-slip process. *Proc Phys Soc* **71**(4): 668–675 (1958)

[6] Brockley C A, Davis H R. The time-dependence of static friction. *J Lubr Technol* **90**(1): 35–41 (1968)

[7] Kato S, Sato N, Matsubayashi T. Some considerations on characteristics of static friction of machine tool slideway. *J Lubr Technol* **94**(3): 234–247 (1972)

[8] Horowitz F G, Ruina A. Slip patterns in a spatially homogeneous fault model. *J Geophys Res Solid Earth* **94**(B8): 10279–10298 (1989)

[9] Ferrero J F, Barrau J J. Study of dry friction under small displacements and near-zero sliding velocity. *Wear* **209**(1–2): 322–327 (1997)

[10] Bureau L, Baumberger T, Caroli C, Ronsin O. Low-velocity friction between macroscopic solids. *Comptes Rendus de l'Académie des Sci Ser IV Phys* **2**(5): 699–707 (2001)

[11] Bowden F P, Tabor D. *The Friction and Lubrication of Solids*. Oxford (UK): Oxford University Press, 1950.

[12] Oldroyd J G. On the formulation of rheological equations of state. *Proc Royal Soc Lond Ser A Math Phys Sci* **200**(1063): 523–541 (1950)

[13] Dieterich J H. Time-dependent friction in rocks. *J Geophys Res* **77**(20): 3690–3697 (1972)

[14] Dieterich J H. Time-dependent friction and the mechanics of stick-slip. *Pure Appl Geophys* **116**(4–5): 790–806 (1978)

[15] Dieterich J H. Modeling of rock friction: 1. Experimental results and constitutive equations. *J Geophys Res Solid Earth* **84**(B5): 2161–2168 (1979)

[16] Ruina A. Slip instability and state variable friction laws. *J Geophys Res Solid Earth* **88**(B12): 10359–10370 (1983)

[17] Rice J R, Ruina A L. Stability of steady frictional slipping. *J Appl Mech* **50**(2): 343–349 (1983)

[18] Popova E, Popov V L. The research works of Coulomb and Amontons and generalized laws of friction. *Friction* **3**(2): 183–190 (2015)

[19] Michałowski R, Mróz Z. Associated and non-associated sliding rules in contact friction problems. *Arch Mech* **30**(3) 259–276 (1978)

[20] Curnier A. A theory of friction. *Int J Solids Struct* **20**(7): 637–647 (1984)

[21] Kikuchi N, Oden J T. *Contact Problems in Elasticity: A Study of Variational Inequalities and Finite Element Methods*. Philadelphia (USA): Society for Industrial and Applied Mathematics, 1988.

[22] Wriggers P. *Computational Contact Mechanics*. Hoboken (USA): John Wiley, 2002.

[23] Hashiguchi K, Ozaki S, Okayasu T. Unconventional friction theory based on the subloading surface concept. *Int J Solids Struct* **42**(5–6): 1705–1727 (2005)

[24] Hashiguchi K, Ozaki S. Constitutive equation for friction with transition from static to kinetic friction and recovery of static friction. *Int J Plast* **24**(11): 2102–2124 (2008)

[25] Hashiguchi K, Ueno M, Kuwayama T, Suzuki N, Yonemura S, Yoshikawa N. Constitutive equation of friction based on the subloading–surface concept. *Proc Royal Soc A* **472**(2191): 20160212 (2016)

[26] Hashiguchi K. *Foundation of Elastoplasticity: Subloading Surface Model*, 3rd edn. Heidelberg (Germany): Springer Nature, 2017.

[27] Ozaki S, Matsuura T, Maegawa S. Rate-, state-, and pressure-dependent friction model based on the elastoplastic theory. *Friction* **8**(4): 768–783 (2020)

[28] Reddy E S, Chapman D N, Sastry V V R N. Direct shear interface test for shaft capacity of piles in sand. *Geotech Test J* **23**(2): 199–205 (2000)

[29] Yang Z X, Jardine R J, Zhu B T, Foray P, Tsuha C H C. Sand grain crushing and interface shearing during displacement pile installation in sand. *Géotechnique* **60**(6): 469–482 (2010)

[30] Abuel-Naga H M, Shaia H A. Interface friction evolution of FRP tube confined concrete piles during the driving installation process. *Géotechnique Lett* **4**(1): 52–56 (2014)

[31] Liu T F, Chen H R, Buckley R M, Quinteros V S, Jardine R J. Characterisation of sand–steel interface shearing behaviour for the interpretation of driven pile behaviour in sands. In: Proceedings of the 7th International Symposium on Deformation Characteristics of Geomaterials, Glasgow, UK, 2019: **92**, 13001.

[32] Tatsuoka F, Molenkamp F, Torii T, Hino T. Behavior of lubrication layers of platens in element tests. *Soils Found* **24**(1): 113–128 (1984)

[33] Ikeda K, Yamakawa Y, Tsutsumi S. Simulation and interpretation of diffuse mode bifurcation of elastoplastic solids. *J Mech Phys Solids* **51**(9): 1649–1673 (2003)

[34] Medina-Cetina Z, Rechenmacher A. Influence of boundary conditions, specimen geometry and material heterogeneity on model calibration from triaxial tests. *Int J Numer Anal Met Geomech* **34**(6): 627–643 (2010)

[35] Bekker M G. *Theory of Land Locomotion*. Ann Arbor (USA): The University of Michigan Press, 1956.

[36] Bekker M G. *Off-the-Road Locomotion*. Ann Arbor (USA): The University of Michigan Press, 1960.

[37] Bekker M G. *Introduction to Terrain-vehicle Systems*. Ann Arbor (USA): The University of Michigan Press, 1969.

[38] Nohse Y, Hashiguchi K, Ueno M, Shikanai T, Izumi H, Koyama F A measurement of basic mechanical quantities of off-the-road traveling performance. *J Terramechanics* **28**(4): 359–370 (1991)

[39] Hashiguchi K, Nohse Y, Ueno M, Sumiyoshi K, Uchiyama K, Yoshimaru T. Travelling performance of a wheel on a finite thickness ground. *J Terramechanics* **31**(4): 257–263 (1994)

[40] Shikanai T, Hashiguchi K, Nohse Y, Ueno M, Okayasu T. Precise measurement of soil deformation and fluctuation in drawbar pull for steel and rubber-coated rigid wheels. *J Terramechanics* **37**(1): 21–39 (2000)

[41] Fukami K, Ueno M, Hashiguchi K, Okayasu T. Mathematical models for soil displacement under a rigid wheel. *J Terramechanics* **43**(3): 287–301 (2006)

[42] Xia K M. Finite element modeling of tire/terrain interaction: Application to predicting soil compaction and tire mobility. *J Terramechanics* **48**(2): 113–123 (2011)

[43] Zhao C L, Zang M Y. Analysis of rigid tire traction performance on a sandy soil by 3D finite element–discrete element method. *J Terramechanics* **55**: 29–37 (2014)

[44] Ozaki S, Hinata K, Senatore C, Iagnemma K. Finite element analysis of periodic ripple formation under rigid wheels. *J Terramechanics* **61**: 11–22 (2015)

[45] Ozaki S, Kondo W. Finite element analysis of tire traveling performance using anisotropic frictional interaction model. *J Terramechanics* **64**: 1–9 (2016)

[46] Spektor M, Solomon N, Malkin S. Measurement of frictional interactions at soil–tool interfaces. *J Terramechanics* **22**(2): 73–80 (1985)

[47] Uesugi M, Kishida H. Influential factors of friction between steel and dry sands. *Soils Found* **26**(2): 33–46 (1986)

[48] Uesugi M, Kishida H. Frictional resistance at yield between dry sand and mild steel. *Soils Found* **26**(4): 139–149 (1986)

[49] Kishida H, Uesugi M. Tests of the interface between sand and steel in the simple shear apparatus. *Géotechnique* **37**(1): 45–52 (1987)

[50] Uesugi M, Kishida H, Tsubakihara Y. Friction between sand and steel under repeated loading. *Soils Found* **29**(3): 127–137 (1989)

[51] Porcino D, Fioravante V, Ghionna V N, Pedroni S. Interface behavior of sands from constant normal stiffness direct shear tests. *Geotech Test J* **26**(3): 289–301 (2003)

[52] Ho T Y K, Jardine R J, Anh-Minh N. Large-displacement interface shear between steel and granular media. *Géotechnique* **61**(3): 221–234 (2011)

[53] Zhou W J, Guo Z, Wang L Z, Li J H, Rui S J. Sand–steel interface behaviour under large-displacement and cyclic shear. *Soil Dyn Earthq Eng* **138**: 106352 (2020)

[54] Butterfield R, Andrawes K Z. On the angles of friction betweens sand and plane surfaces. *J Terramechanics* **8**(4): 15–23 (1972)

[55] Yao Y S, Zeng D C. Investigation of the relationship between soil–metal friction and sliding speed. *J Terramechanics* **27**(4): 283–290 (1990)

[56] McKyes E. Investigation of the relationship between soil–metal friction and sliding speed: Yao Yusu and Zeng Dechao, J. Terramechanics **27**(4), 283–290 (1990). *J Terramechanics* **29**(2): 281–282 (1992)
[57] Han F, Ganju E, Salgado R, Prezzi M. Effects of interface roughness, particle geometry, and gradation on the sand–steel interface friction angle. *J Geotech Geoenviron Eng* **144**(12): 04018096 (2018)
[58] Sandeep C S, Senetakis K. Micromechanical experiments using a new inter-granule loading apparatus on gravel to ballast-sized materials. *Friction* **8**(1): 70–82 (2020)
[59] Zhang H J, Liu S H, Xiao H P. Sliding friction of shale rock on dry quartz sand particles. *Friction* **7**(4): 307–315 (2019)
[60] Zhang X J, Sun W, Wang W, Liu K. Experimental investigation of granular friction behaviors during reciprocating sliding. *Friction* **10**(5): 732–747 (2022)
[61] Truesdell C. The simplest rate theory of pure elasticity. *Commun Pure Appl Math* **8**(1): 123–132 (1955)
[62] Truesdell C, Noll W. *The Non-linear Field Theories of Mechanics*. Berlin: Springer Nature, 1965.
[63] Simo J C, Hughes T J R. *Computational Inelasticity*. New York: Springer Science & Business Media, 1998.
[64] De Souza Neto E A, Perić D, Owen D R J. *Computational Methods for Plasticity: Theory and Applications*. Chichester (UK): John Wiley and Sons Ltd, 2008.
[65] Kojić M, Bathe K J. Studies of finite element procedures—Stress solution of a closed elastic strain path with stretching and shearing using the updated Lagrangian Jaumann formulation. *Comput Struct* **26**(1–2): 175–179 (1987)
[66] Brepols T, Vladimirov I N, Reese S. Numerical comparison of isotropic hypo- and hyperelastic-based plasticity models with application to industrial forming processes. *Int J Plast* **63**: 18–48 (2014)
[67] Perić D. On consistent stress rates in solid mechanics: Computational implications. *Int J Numer Methods Eng* **33**(4): 799–817 (1992)
[68] Yoshimi Y, Kishida T. A ring torsion apparatus for evaluating friction between soil and metal surfaces. *Geotech Test J* **4**(4): 145–152 (1981)

Toshiyuki OZAKI. He received his Ph.D. degree from Kyushu University, Japan, in 2005, and he has been working for Kyushu Electric Engineering Consultants, Inc., Japan, since 1994. His current position is a director at the design of transmission line foundation department. He works not only on the design of civil engineering structures, but also on the design of the counter measures against slope failure.

Yuki YAMAKAWA. He studied civil engineering (1992–2000) in Tohoku University, Japan, and received his Ph.D. degree in 2003 from Tohoku University, Japan. He worked as a research associate in Nagaoka University of Technology, Japan, in 2000–2005. His current position is an associate professor at the Department of Civil and Environmental Engineering in Tohoku University, Japan. His research area covers the nonlinear continuum mechanics for solids, theory and computation of elastoplasticity, and computational geomechanics.

Masami UENO. He received his Ph.D. degree of agriculture from the University of Tsukuba, Japan, in 1983. He had worked in the Department of Agricultural Engineering, University of the Ryukyus, Japan. He retired in 2014, and is the Professor Emeritus of the University. His research covers the smart farming, the systems engineering for agriculture, and the solid mechanics.

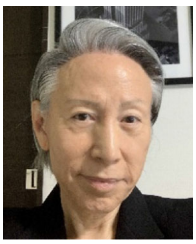

Koichi HASHIGUCHI. He received his Ph.D. degree from Tokyo Institute of Technology, Japan, in 1976. After that he served as an assistant professor, associate professor, and professor at Kyushu University, Japan. He is currently the Professor Emeritus in Kyushu University, Japan and affiliate member of the Science Council of Japan. His research area covers elastoplastic deformation and friction phenomena of solids, proposing the subloading surface model.